Parallel Hybrid Electric Vehicle Energy Control Exploiting an Integrated Topology of Multi-Drives

1 G. Esha 2.Dr. N. Ramchandra 3 Voruganti Bharath kumar 4 V.Vishnuvardhan

1,3,4 Assistant Professor in Department of Electrical and Electronics Engineering

2 Professor in Department of Electrical and Electronics Engineering

1,2,3,4 St.Martin's Engineering College, Secunderabad, Telangana, India

Keywords: Automotive, current vector control, hybrid electric vehicles, hybrid energy storage, induction motor drives.

Abstract

The main purpose of this paper is to provide a comprehensive study of an online energy management strategy devoted to hybrid electric vehicle (HEV) parallel drivetrains adopting an integrated multi-drives topology to interface a multi winding induction machine with the on-board hybrid storage units. This solution is designed to allow multi-directional power flows among the storage units and the drivetrain. Basically, the proposed efficiency optimization method continuously searches for the best compromise between the torque demand, system efficiency and power capability of each storage unit. The considered electric drive configuration allows to effectively and independently handle the power flowing in storage units featuring different sizes and DC voltages, while improving the overall reliability. A good agreement between simulations and experimental results is achieved.

1. Introduction

The energy management of the electrical machine and storage systems in hybrid electric vehicles (HEV) is a very hot topic among academic researchers and industry manufactures. Several approaches devoted to parallel drivetrains have been introduced by many authors, considering from time to time different control strategies and constraints depending on the specific application [1-6]. In most cases, the storage system is hybrid since it includes supercapacitors and batteries, both assembled by suitable electric connections of a certain number of cells.

The battery pack of a conventional Hybrid Energy Storage Systems (HESS) installed in HEV is directly connected to the DC link while a half bridge DC/DC converter is usually placed between the supercapacitors bank and the DC link, [1]. Such configuration implies that the DC/DC power converter must match the maximum power level of the supercapacitors bank to sustain large current peaks. Furthermore, because of the shared voltage DC bus, any voltage variation in the bus negatively affects the management strategy of both storage units, [2]. With regards to the system reliability, a fault in the AC/DC power converter of the conventional topology or in a single winding of the electrical machine (open phase fault) compromises the entire delivering power flow and thus the charging and discharging procedures in all the storage units.

A fuzzy logic controller and a model predictive algorithm are presented in [2] to improve the peak power compensation provided by the supercapacitor limiting the DC voltage large variations while reducing the battery pack current stress. In [3] the proposed control strategy exploits a frequency approach to manage the energy flows in storage units.

In this paper an integrated multi-drives (IMD) topology is exploited to ensure an online and parallel multi-directional power flows among the storage units and the drivetrain. Thanks to the turns ratio of the induction machine windings, storage units featuring different sizes and DC voltage levels can be easily connected, avoiding the use of more DC/DC power converters and leading to an increment of the system reliability.

2. Integrated Multi-Drives Topology

The IMD configuration considered in this paper is displayed in Fig. 1. The conventional winding of a standard squirrel cage induction machine is split into different three-phase sub-windings, keeping the same original mmf distribution. The windings feature a different number of turns N_j strictly related to the desired back emf, while the wire cross sections are related to their nominal currents.

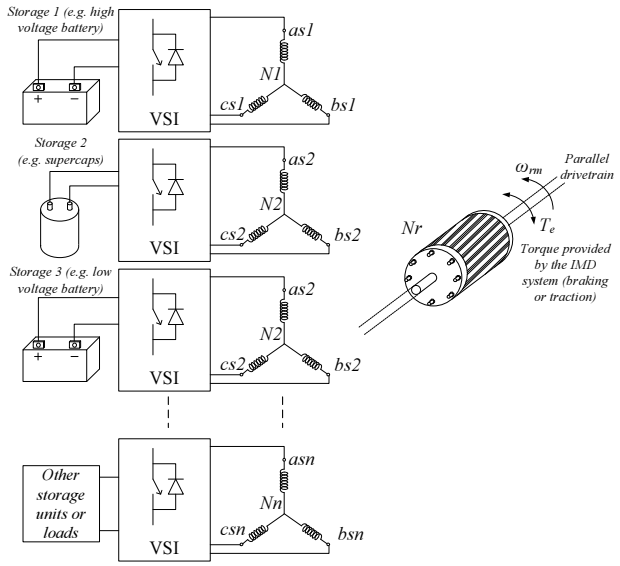

Fig. 1. IMD with multiple DC storage units.

The total magnetic airgap flux and the torque generated in the electromagnetic system can be approximated (by considering the assumption of linear system) to that achievable by combining the contribution provided by the fictitious sub-motors (SM), each one consisting of one of the stator sub-

windings and sharing the same rotor. This electromagnetic system allows supplying more storage units featuring different capacities and DC voltage levels by means of standard three-phase voltage source inverters (VSI).

According to [7-9] the IMD can be easily controlled by implementing *n* decoupled indirect field oriented control (IFOC) algorithms in the SMs, adopting the same *qd* reference frame for all the drives composing the IMD. The field orientation in each unit is obtained by imposing the total slip angular frequency $\omega_{s\lambda r}$ equal to:

$$\omega_{s\lambda r} = \frac{1}{\tau_r}\left(i_{qs1} + i'_{qs2} \ldots + i'_{qsn}\right) / \left(i_{ds1} + i'_{ds2} \ldots + i'_{dsn}\right) \quad (1)$$

where τ_r is the rotor time constant, while i_{qsj} and i_{dsj} are the torque and flux components of the stator current vectors flowing in the *j-th* SM. It is worth noting that in this analytical formulation the electrical quantities associated to the *j-th* stator winding (and to the rotor) are referred to the stator winding *1* through the turns ratio N_1/N_j (N_1/N_r for the rotor). The rotor flux angular position $\theta_{\lambda r}$ is calculated from $\omega_{s\lambda r}$ and rotor speed ω_{re} as:

$$\theta_{\lambda r} = \theta_{\lambda r0} + \int\left(\omega_{s\lambda r} + \omega_{re}\right)dt\ ,\ \omega_{re} = \overline{p}\,\omega_{rm} \quad (2)$$

where *p* indicates the pole pairs. The total electromagnetic torque provided by the IMD is given by (3), as the sum of the torque contributions provided by each SM:

$$\begin{aligned} T_e &= \frac{P_m}{\omega_{rm}} = \frac{3}{2}\overline{p}\left(i_{qs1} + \ldots. + i'_{qsn}\right)\lambda'_{dr} = \\ &= \frac{3}{2}\overline{p}L_M\left(i_{qs1} + \ldots + i'_{qsn}\right)\cdot\left(i_{ds1} + \ldots + i'_{dsn}\right) = \\ &= T_{e1} + \ldots + T_{en} \end{aligned} \quad (3)$$

where:

$$T_{ej} = \frac{3}{2}\overline{p}L_M i'_{qsj}\left(i_{ds1} + \ldots + i'_{dsn}\right) \quad (4)$$

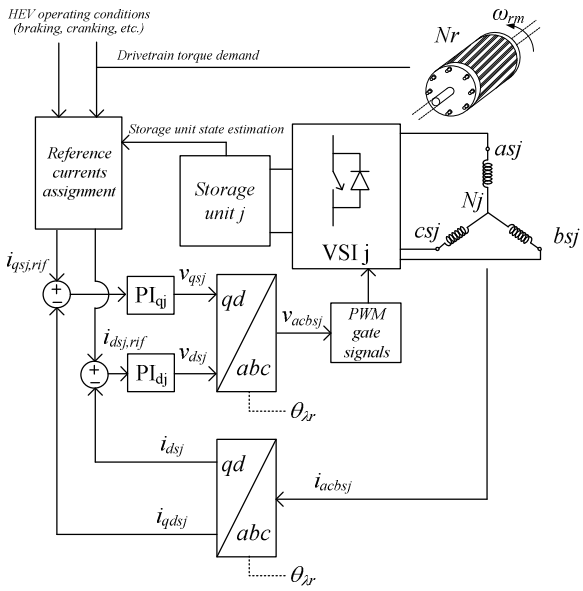

Fig. 2. Block diagram of the IFOC control for the *j-th* SM.

The rotor flux in the electrical machine can be calculated as:

$$\lambda'_{dr} = L_M\left(i_{ds1} + \ldots + i'_{dsn}\right) \quad (5)$$

Hence, under field orientation, the torque produced by the *n* integrated motors is directly proportional to the algebraic sum of the torque components i_{qsj}, while the amplitude of the flux is given by the algebraic sum of the flux components associated to i_{dsj}.

Fig. 2 displays a block diagram of the IFOC implemented in the *j-th* SM. The current loop allows to handle the decoupled torque and flux controls in each SM. The reference currents are assigned on the basis of the actual operating scenario (braking, cranking, etc.) and storage state, as detailed in the following sections.

3. Storage Units Modeling

The storage units used in HEV parallel drivetrains are mainly strings of supercapacitors and battery packs (both lead-acid or lithium-ions technologies).

The accurate knowledge of the actual State of Charge *SOC* and power capability *PC* of each single storage unit can be very significant to assess the suitable energy management of the entire system [10-12].

Supercapacitors strings can be represented by a simple RC network, as proposed in technical literature and in datasheets of supercapacitors's manufacturers [13]. The capacitor C_{sc} and resistor ESR_{sc} composing the RC network can be easily identified using data provided by the manufacturers:

$$\begin{aligned} C_{sc} &= C_{sc,cell} / n_{sc} \\ ESR_{sc} &= ESR_{sc,cell} \cdot n_{sc} \\ v_{sc} &= v_{sc,cell} \cdot n_{sc} \\ v_{sc,rated} &= v_{sc,cell,rated} \cdot n_{sc} \end{aligned} \quad (6)$$

where n_{sc} is the number of cells, the State of Charge associated to supercapacitors SOC_{sc} is the ratio between the actual voltage and the maximum voltage:

$$SOC_{sc} = \frac{v_{sc}}{v_{sc,max}} \quad (7)$$

Generally, the maximum voltage value is assigned equal to the rated one. The SOC_{sc} is usually maintained between 50% ($SOC_{sc,min}$) and 95% ($SOC_{sc,max}$) [1]. The power capability of the supercapacitor during the charge process is function of the actual SOC_{sc} and selected horizon time Δt, the last depending on the operating scenario of the drivetrain (braking, acceleration, etc.) [14],[15]:

$$PC_{sc,ch} = i_{sc,ch,PC} \cdot \left(\left|\frac{SOC_{sc} - SOC_{sc,max}}{2}\right| + SOC_{sc}\right) \cdot v_{sc,max} \quad (8)$$

where $i_{sc,ch,PC}$ is the maximum value of the current that can be imposed during the charging process at a given actual SOC_{sc} and maximum $SOC_{sc,max}$:

$$i_{sc,ch,PC} = \frac{SOC_{sc} - SOC_{sc,max}}{\Delta t} v_{sc,max} \cdot C_{sc} \quad (9)$$

Similar formulation can be used during the discharging process:

$$PC_{sc,ds} = i_{sc,ds,PC} \cdot \left(SOC_{sc} - \left| \frac{SOC_{sc} - SOC_{sc,min}}{2} \right| \right) \cdot v_{sc,max} \quad (10)$$

$$i_{sc,ds,PC} = \frac{SOC_{sc} - SOC_{sc,min}}{\Delta t} v_{sc,max} \cdot C_{sc} \quad (11)$$

The amount of losses in the supercapacitors is calculated considering the Joule loss associated to the resistance ESR_{sc}:

$$P_{l,sc} = \left(ESR_{sc}\right) \cdot i_{sc}^2 \quad (12)$$

Differently than supercapacitors, modeling of batteries is more complicated due to several non-linear phenomena occurring during charging and discharging processes. Moreover, the battery behavior is strongly affected by the State of Health (*SOH*), load variations and environmental conditions, [16].

In this analysis the battery pack has been modeled by using the Thevenin equivalent circuit [17-18], while the battery SOC_{bt} has been estimated exploiting a PI-based observer scheme, [19]. The controller parameters have been chosen in order to match the automotive dynamics. Thanks to such online algorithm, an accurate SOC_{bt} estimation is provided.

A good accuracy in the power capability prediction $PC_{bt,ds}$ during the discharging process can be obtained by taking into account the rate limits depending on the actual SOC_{bt} [20], and a suitable time horizon Δt:

$$PC_{bt,ds} = v_{bt,min} \cdot i_{bt,ds,PC} \quad (13)$$

where:

$$i_{bt,ds,PC} = \frac{SOC_{bt} - SOC_{bt,min}}{\Delta t} \cdot SOH \cdot C_{bt} \quad (14)$$

C_{bt} is the rated capacity of the battery. It is worth noting that all the quantities included in (13) and (14) are continuously provided by the PI-based observer scheme, [19].

A similar formulation can be adopted for the charging process, in which the additional nonlinear phenomena and the significant dependency from the actual current rate are taken into account by introducing an additional correction term, [21]. Hence, the power capability during charge $PC_{bt,ch}$ can be calculated as:

$$PC_{bt,ch} = v_{bt,max} \cdot i_{bt,ch,PC} \cdot \eta_{ch} \quad (15)$$

Another constraints regarding the charging process is related to the charging current $i_{bt,ch}$ recommended by the battery manufacturer pursuing the objective to extend lifetime, [17]. The selected charging current $i_{bt,ch}$ is usually lower than the one related to the power calculated from capability assessment, $i_{bt,ch,PC}$:

$$i_{bt,ch} < i_{bt,ch,PC} \quad (16)$$

In most cases a constant current (CC) control strategy is implemented for SOC_{bt} lower than 70-75%, while a constant voltage (CV) regulation for higher SOC_{bt} values.

In case of very high SOC_{bt} values occurring during CV regulation, if the restored energy exceeds the rated capacity a dangerous overcharge could happen [22]. It is necessary to avoid frequently overcharge states since the *SOH* of the battery rapidly decreases yielding to permanent damages. To avoid such drawbacks, the implementation of the considered real-time SOC_{bt} estimation scheme is necessary as well as the information provided by the manufacturer about the CV regulation.

As for the supercapacitors, also for batteries the losses estimation can be calculated by considering Joule losses associated to the resistive elements:

$$P_{l,bt} = \left(R_i + R_t\right) \cdot i_{bt}^2 \quad (17)$$

For safety reasons, a resistive braking system in parallel to the supercapacitor as well as to the battery is usually included in the system. During normal operation, this resistive braking is inactive [23].

4. Energy Management Control Strategy

After having provided some technical constraints regarding the charging and discharging processes of storage units, a straightforward control strategy for the IMD system is described hereafter. The main goal of the proposed control strategy is to increase the flexibility and efficiency of the transferring power among the storage units and the HEV parallel drivetrain.

Different operating scenarios of the HEV power drivetrain have been considered. Although the proposed approach can be applied to any combination of storage technologies and number of units, the IMD considered in this study includes two SMs connected to two different storage units: (1) a battery pack and (2) a supercapacitors string. For each operating scenario, the cooperative control strategy acts in order to select the optimal set of reference *qd* currents allowing to handle in the most suitable way the power flows in the system. Focusing on the braking scenario depicted in Fig. 3, the demanded torque $T_{e,demand}$ has been assessed taking into account the typical profile shown in Fig. 4, [24].

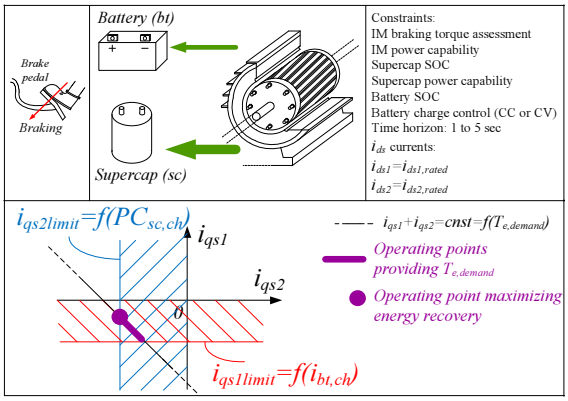

Fig. 3. Braking scenario.

The torque $T_{e,demand}$ represents a contribution of the overall braking torque, in addition to hydraulic, frictional and engine braking. The rotor speed profile is obtained by considering the Newton's second law applied to the parallel drivetrain, [24].

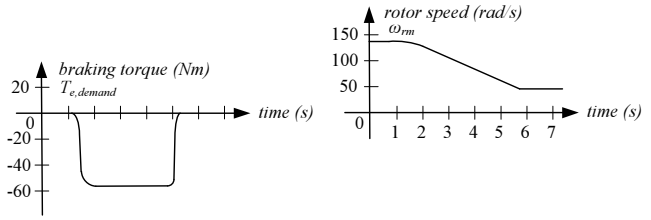

Fig. 4. Reference profiles for the demanded torque $T_{e,demand}$ and for the rotor speed ω_{rm} during braking.

With regards to the reference currents on d axis i_{ds1} and i_{ds2}, they have been imposed equal to their rated values in order to allow a fast dynamic response during starter and generation operations. On the contrary, the reference currents on the q axis i_{qs1} and i_{qs2} have to be selected to satisfy different technical constraints related to demanded torque $T_{e,demand}$ and the maximum currents allowed $i_{qs1limit}$ and $i_{qs2limit}$ for the considered storage technologies:

$$\begin{cases} i_{qs1} + i_{qs2} = \dfrac{T_{e,demand}}{\dfrac{3}{2}\overline{p}L_M\left(i_{ds1,rated} + i_{ds2,rated}\right)} \\ T_{e,demand} \cdot \omega_{rm,t0} = PC_{IM} \\ \left|i_{qs1}\right| \le \left|i_{qs1limit}\right| \quad i_{qs1limit} = f(i_{bt,ch}) = (19) \\ i_{qs2} = i_{qs2limit} \quad i_{qs2limit} = f(PC_{sc,ch}) = (20) \end{cases} \tag{18}$$

In particular, the sum $i_{qs1} + i_{qs2}$ is strictly related to the required torque $T_{e,demand}$, while $\omega_{rm,t0}$ represents the initial rotor speed. PC_{IM} is the power capability of the induction machine, usually assigned equal to the rated power $P_{rated,IM}$. The current $i_{qs1limit}$ is function of the maximum charging current that can be forced into the battery $i_{bt,ch}$ according to manufacturer's recommendations as in (16). By assuming that mechanical, iron and power inverter losses can be considered negligible, the current $i_{qs1limit}$ can be approximated in a straightforward way as:

$$i_{qs1limit} = \frac{v_{bt,ch} \cdot i_{bt,ch}}{\dfrac{3}{2}\overline{p}L_M\left(i_{ds1,rated} + i_{ds2,rated}\right)\omega_{rm,t0}} \tag{19}$$

The current $i_{qs2limit}$ is a function of the supercapacitor power capability $PC_{sc,ch}$ referred to the charging process. Considering the above mentioned assumptions, even the current $i_{qs2limit}$ can be easily calculated as:

$$i_{qs2limit} = \frac{PC_{sc,ch} + P_{l,sc}}{\dfrac{3}{2}\overline{p}L_M\left(i_{ds1,rated} + i_{ds2,rated}\right)\omega_{rm,t0}} \tag{20}$$

The evaluation of supercapacitor power capability $PC_{sc,ch}$ is performed by using (8), considering the actual SOC_{sc} estimation provided by (7) and a typical time horizon Δt of 5 s for the braking operation, [24]. The working point of the IMD is thus established according to (18), complying with all the aforementioned constraints. Finally, Fig. 3 displays all viable operating points satisfying the demanded torque $T_{e,demand}$ and the working point allowing to extract the maximum energy during braking while satisfying the operating limits associated to the storage units technologies. It is worth noting the simplicity of the control structure to reflect the current limits of the storage units in terms of limits in the torque and flux current components associated to each SM composing the IMD.

Similar control strategies can be implemented in the IMD for the other working scenarios reported in Figs. 5-9, by including different technical constraints.

In particular, during the brake release scenario, displayed in Fig. 5, the current $i_{qs1limit}$ is assigned considering (19). On the contrary, the current $i_{qs2limit}$ is related to the actual power capability of the supercapacitor $PC_{sc,ds}$ during the discharging process:

$$i_{qs2limit} = \frac{PC_{sc,ds} + P_{l,sc}}{\dfrac{3}{2}\overline{p}L_M\left(i_{ds1,rated} + i_{ds2,rated}\right)\omega_{rm,t0}} \tag{21}$$

The reference currents on d axis i_{ds1} and i_{ds2} have to be established equal to their rated values, while the sum $i_{qs1} + i_{qs2}$ is null since no active power flows towards the rotor.

This scenario is not convenient from an energetic point of view because the power conversion requires a double stage: DC to AC quantities (supercapacitor to machine) and AC to DC quantities (machine to battery). However, it represents an optimal solution for safety reasons, whenever it is necessary to discharge the supercapacitor as the SOC_{sc} is close to its maximum level.

The relationships (22) summarize the technical constraints considered for this working mode.

$$\begin{cases} i_{qs1} + i_{qs2} = 0 \\ \left|i_{qs1}\right| \le \left|i_{qs1limit}\right| \quad i_{qs1limit} = f(i_{bt,ch}) = (19) \\ i_{qs2} \le i_{qs2limit} \quad i_{qs2limit} = f(PC_{sc,ds}) = (21) \end{cases} \tag{22}$$

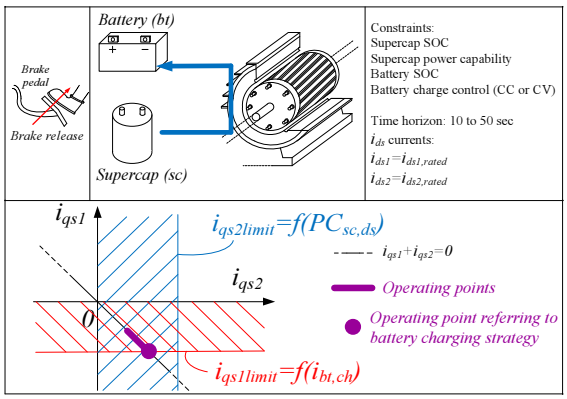

Fig. 5. Brake release scenario.

During the acceleration scenario both storage units transfer active power towards the mechanical system, under the technical constraints indicated in (23).

Both the limits on q axis i_{qsj} currents are related to the power capability of the storage units. Hence, the allowed operating range, which is highlighted in Fig. 6, depends on the actual SOC of each storage unit.

$$\begin{cases} i_{qs1}+i_{qs2}=\dfrac{T_{e,demand}}{\dfrac{3}{2}\overline{p}L_M\left(i_{ds1,rated}+i_{ds2,rated}\right)} \\ T_{e,demand}\le T_{IM,rated} \\ i_{qs1}\le i_{qs1limit} \quad i_{qs1limit}=f(PC_{bt,ds})=(24) \\ i_{qs2}\le i_{qs2limit} \quad i_{qs2limit}=f(PC_{sc,ds})=(25) \end{cases} \tag{23}$$

with:

$$i_{qs1limit}=\frac{PC_{bt,ds}+P_{l,bt}}{\dfrac{3}{2}\overline{p}L_M\left(i_{ds1,rated}+i_{ds2,rated}\right)\omega_{rm,rated}} \tag{24}$$

and:

$$i_{qs2limit}=\frac{PC_{sc,ds}+P_{l,sc}}{\dfrac{3}{2}\overline{p}L_M\left(i_{ds1,rated}+i_{ds2,rated}\right)\omega_{rm,rated}} \tag{25}$$

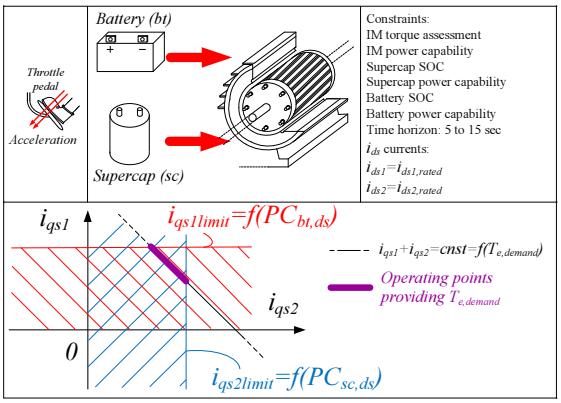

Fig. 6. Acceleration scenario.

Even under this working condition the reference currents on d axis i_{ds1} and i_{ds2} have been forced equal to their rated values. The sum i_{qs1} + i_{qs2} is proportional to the required torque $T_{e,demand}$. In such scenario, the final speed is larger than the initial. Unfortunately, the final speed in usually not known in advance. For safety reasons regarding the current limits, a viable way to assess the rotor speed is to assign its rated value, as in (24) and (25).

Whenever the vehicle is moving at constant speed exploiting a regenerative scenario, the analytical formulation can be expressed by:

$$\begin{cases} \left|i_{qs1}\right|\le\left|i_{qs1limit}\right| \\ i_{qs1limit}=f(i_{bt,ch})=(19) \\ i_{qs2}=0 \end{cases} \tag{26}$$

The reference currents on d axis i_{ds1} and i_{ds2} are equal to the rated ones. The reference current i_{qs1} can be calculated by (19) complying with the manufacturer recommendations.

Under certain conditions, the reference current i_{qs2} could be imposed at a value less than zero, thus transferring an amount of energy to the supercapacitor. In such a case, the analytical formulation is similar to that associated to the braking case but a longer time horizon has to be assigned. However, due to such longer time horizon, the supercapacitor could reach a SOC_{sc} value close to the maximum level, leading to the necessity to discharge the supercapacitor in order to get ready for a future recharge.

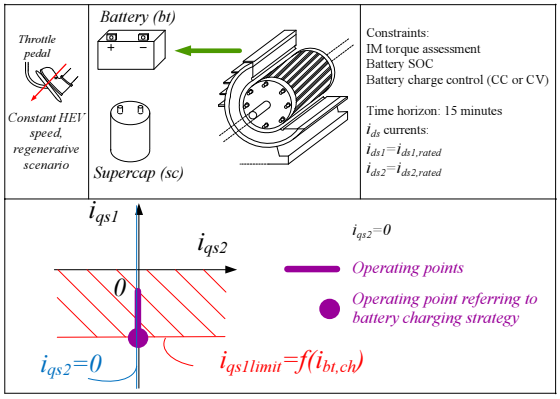

Fig. 7. Constant HEV speed, regenerative scenario.

Differently than last operating condition, when the vehicle is moving at constant speed it could be raise the possibility to supply the mechanical system from the storage units (fuel saving scenario); in that case the technical constraints are:

$$\begin{cases} i_{qs1}+i_{qs2}=\dfrac{T_{e,demand}}{\dfrac{3}{2}\overline{p}L_M\left(i_{ds1}+i_{ds2}\right)} \\ T_{e,demand}\le T_{IM,rated} \\ i_{qs1}\le i_{qs1limit} \quad i_{qs1limit}=f(PC_{bt,ds})=(24) \\ i_{qs2}\le i_{qs2limit} \quad i_{qs2limit}=f(PC_{sc,ds})=(25) \\ (i_{qs1},i_{qs2},i_{ds1},i_{ds2})=(i^*_{qs1},i^*_{qs2},i^*_{ds1},i^*_{ds2}) \\ (i^*_{qs1},i^*_{qs2},i^*_{ds1},i^*_{ds2})\rightarrow max\ efficiency \end{cases} \tag{27}$$

Here the main goal is to maximize the efficiency in order to get a significant fuel saving. Hence, the currents with superscript * represent the best set in terms of losses reduction, including the losses on battery and supercapacitor. The identification of these currents is not the focus of this study.

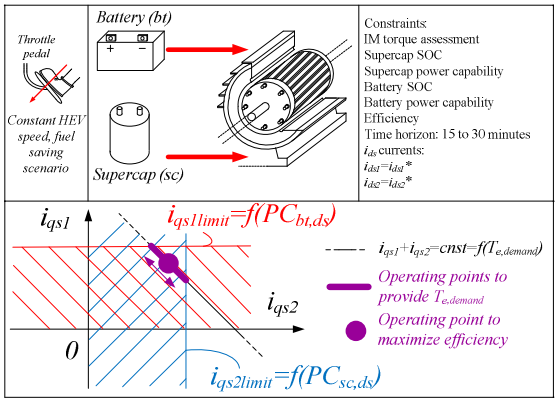

Fig. 8. Constant HEV speed, fuel saving scenario.

The current $i_{qs1limit}$ can be calculated by (24), since it depends on the PC_{bt} during discharge. The value $i_{qs2limit}$ is related to the $PC_{sc,ds}$ and it can be calculated by (25).

The amount of energy necessary to crank the engine is usually provided by the battery. A temporary increase in maximum voltages and currents can be accepted in the battery pack depending on the value of the demanded cranking torque $T_{e,cranking}$. The value $i_{qs1limit}$ depends on actual $PC_{bt,ds}$. If the actual $PC_{bt,ds}$ is too low, thanks to the proposed IMD, the supercapacitor could be used in place of the battery. In this case the torque components of the stator current are given by:

$$\begin{cases} i_{qs2} = 0 \\ i_{qs1} = \dfrac{T_{e,cranking}}{\dfrac{3}{2}\overline{p}L_M\left(i_{ds1,rated} + i_{ds2,rated}\right)} \\ i_{qs1} \le i_{qs1limit} \qquad i_{qs1limit} = f(PC_{bt,ds}) = (24) \end{cases} \tag{28}$$

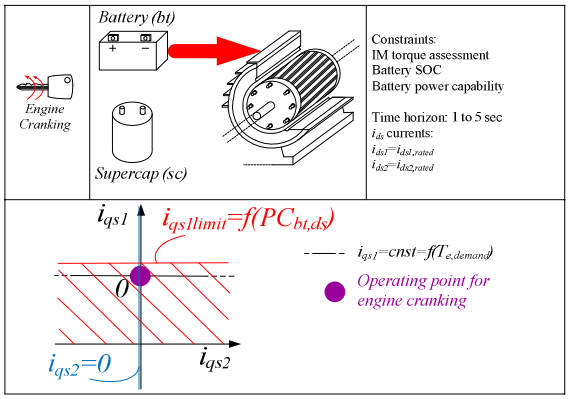

Fig. 9. Engine cranking scenario.

5. Simulations and Experimental Validation

The validation of the proposed energy management strategy for HEV parallel drivetrains has been conducted through simulations as well as experimental tests.

(a).Simulations:

The simulations have been implemented considering a scaled reduced-power system. Technical data of the main components composing the simulated IMD system are summarized in Table 1.

Table 1 Technical specifications of IMD and storage units.

Multi Winding Induction Machine 2.2 kW		***SM₁***	***SM₂***
Rated Voltage (V)		266	133
Rated Frequency (Hz)		50	50
Rated speed (rpm)		1470	1470
Rated current (A)		4.86	4.86
Storage Unit 1 - Battery (n_{bt} 24 V batteries in series)		***Storage Unit 2 - Supercap (n_{sc} 16 V supercapacitors in series)***	
Rated Voltage (V)	24	Rated Voltage (V)	16
Rated Capacity (Ah)	7.2	Rated Capacity (F)	9.5
n_{bt}	19	*ESR* (mΩ)	5.3
Technology	VRLA	n_{sc}	19

A random driving cycle including the considered scenarios is shown in Fig. 10. The reference *qd* currents are calculated by using the analytical formulations described above.

Table 2 Numerical Resolution of system (18)

a.	PC_{IM}=2.2 kW, $\omega_{rm,t0}$=135 rad/s → $T_{e,demand}$=16.3 Nm
b.	i_{ds1}= $i_{ds1,rated}$=1.84 A, i_{ds2}= $i_{ds2,rated}$=0.5 A
c.	$T_{e,demand}$, i_{ds1}, i_{ds2} → i_{qs1}+i_{qs2}≈10 A
d.	$SOC_{bt,t0}$=60% → $i_{bt,ch}$≈1 A → $i_{qs1limit}$≈2.75 A
e.	Δt=5 s, $SOC_{sc,t0}$=80%, $SOC_{sc,max}$=95% → → $PC_{sc,ch}$≈1300 W → $i_{qs2limit}$≈7.5 A
f.	*q* axis reference currents: i_{qs1}=2.5 A, i_{qs2}=7.5 A

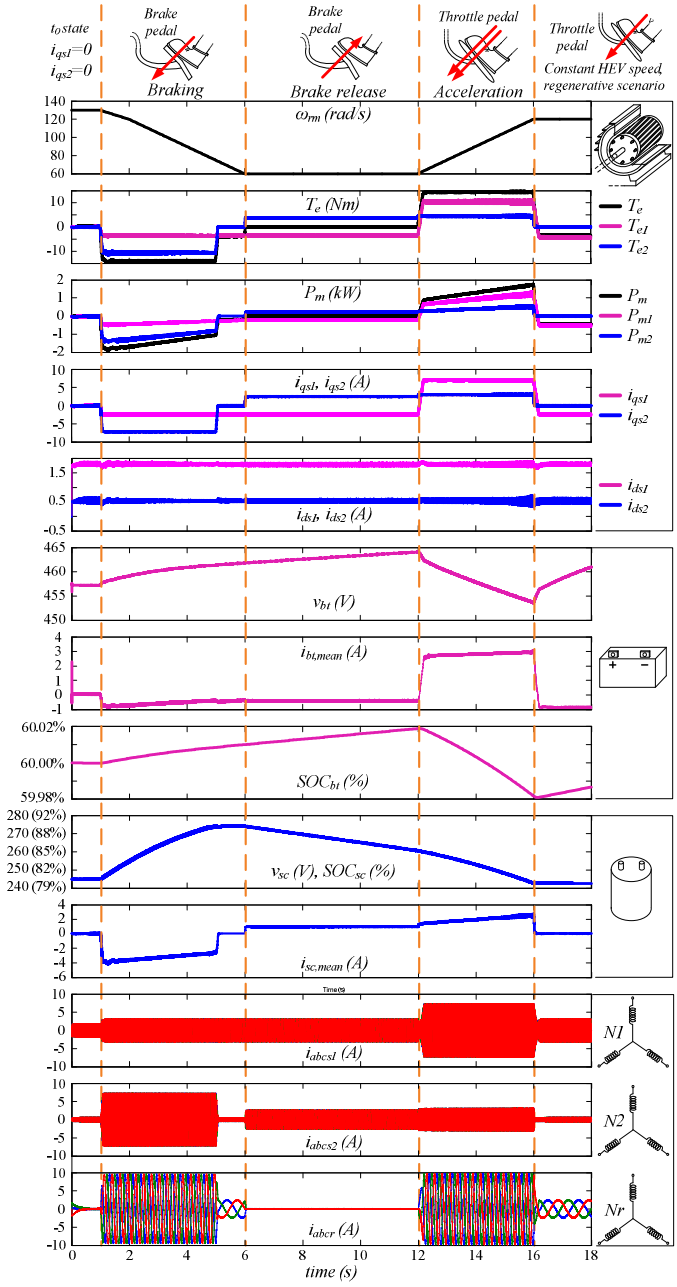

Fig. 10. Simulation of random driving cycles including the analyzed operating scenarios.

For instance, during the braking interval from 1 s to 6 s, the numerical resolution of the system (18) is in Table 2.
In the next period starting from 6 s to 12 s, the power is directed from the supercapacitor to the battery pack. It can be observed that the charge current of battery is still kept constant, equal to the previous step. In this case, a CC regulation is implemented with a low current level, according to the battery datasheet. The SOC_{sc} decreases because of the energy transferred between the storage units. In this way the supercapacitor is discharged in the expectation of a possible subsequent recharge. From 12 s to 16 s, the supercapacitor is again forced to discharge because of an acceleration of the vehicle. It can be observed that, due to the actual $PC_{bt,ds}$ and $PC_{sc,ds}$ values, the bigger contribution in terms of electromagnetic torque is provided by the SM supplied from the battery. In the final period starting from 16 s to the end of simulation, the battery is again recharged performing a CC regulation while no energy flows to the supercapacitor.

(b).Experimental tests:
Experimental analysis has been conducted in order to verify the effectiveness of the proposed control strategy for the IMD. In the experimental test bench, the machine is the same multi winding induction motor that has been previously used in the simulations, whose technical data are summarized in Table 1. The storage unit 1 is a 120 V 27 Ah VRLA battery pack, while the storage unit 2 consists of a 84 V 27 Ah VRLA battery pack. In the experimental setup, the drivetrain is mechanically coupled to another induction motor drive in which a IFOC is implemented to impose a given speed profile over time, [25].

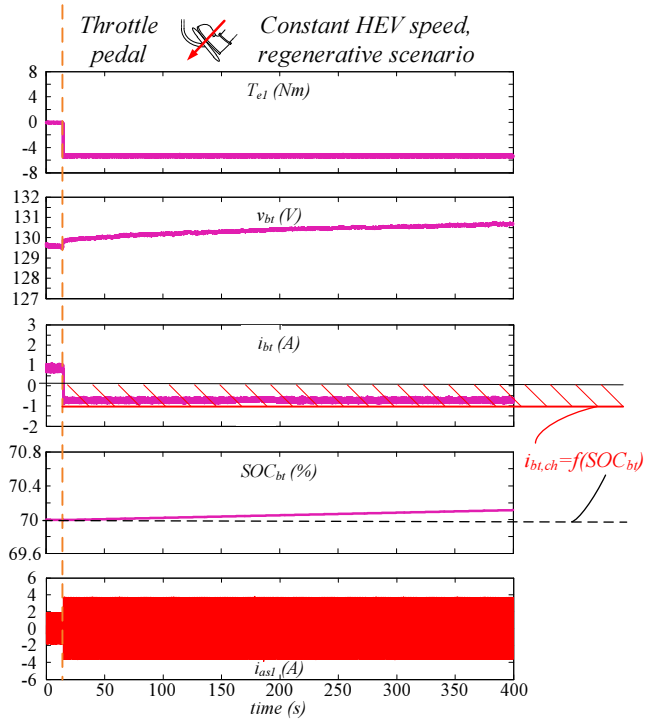

Fig. 11. Experimental test. Regenerative scenario at constant HEV speed; the initial SOC_{bt} of the storage unit 1 is close to 70% of its rated value.

For the sake of example, Fig. 11 shows the main mechanical and electrical quantities acquired considering the operating scenario represented in Fig. 7 and in the last part of the simulation of Fig. 10 (16 s to 18 s). In such a case, the HEV travels at a quasi-constant speed (e.g. in a highway) with a time horizon of several minutes.
A certain amount of regenerative energy can be obtained from the drivetrain and used to recharge the storage unit 1, while no energy flows towards the storage unit 2. The main constraint is related to the $PC_{bt,ch}$ i.e. to the charge current $i_{bt,ch}$ according to the relationships (15) and (16).
The value of $i_{bt,ch}$ is given by the battery manufacturer as a function of the actual SOC_{bt}. This circumstance is pointed out in Fig. 11. Since the actual SOC_{bt} is about 70%, in the battery datasheet the recommended control is the CC regulation while the optimal charge current for a long time horizon is fixed to about 1 A. In Fig. 11 it can be observed that these constraints are respected. The currents i_{qs1}, i_{ds1}, i_{qs2} and i_{ds2} have the same values used in simulations i.e. the same values reported in Fig. 10 from 16 s to 18 s.
Fig. 12 shows a similar operating scenario but with a greater SOC_{bt} value. Due to the long term horizon (several minutes) the $PC_{bt,ch}$ estimation needs to be frequently updated since it could decrease very fast while SOC_{bt} increases.
In Fig. 12 it can be observed that each $PC_{bt,ch}$ update, occurring while SOC_{bt} increases, leads to a decrease in the value assigned for i_{qs1}.

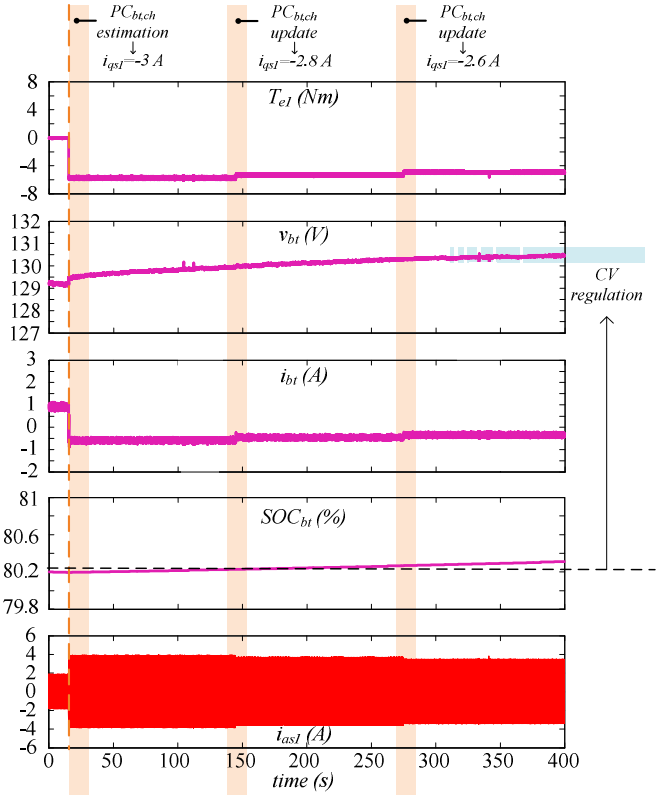

Fig. 12. Experimental test. Regenerative scenario at constant HEV speed; the initial SOC_{bt} of the storage unit 1 is close to 80% of its rated value.

Furthermore, this control strategy satisfies the battery datasheet recommendations. In fact, since the actual SOC_{bt} is about 80%, it is recommended by the manufacturer to progressively reduce the charge current until reaching a CV regulation state, as highlighted in Fig. 12 on the right part of the battery voltage waveform.

Fig. 13 shows an example of brake release scenario, described in Fig. 5 and in (22). No active power flows towards the rotor. The energy flows from the storage unit 1 to the storage unit 2. In fact, the voltage of battery pack 1 decreases while, at the same time, the voltage of battery pack 2 increases.

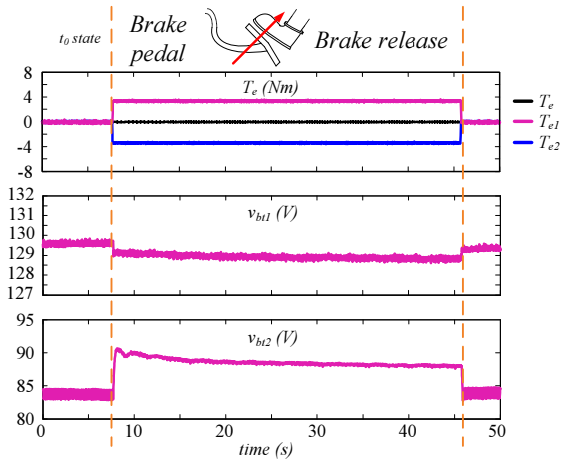

Fig. 13. Experimental test. Brake release scenario.

5. Conclusions

This paper deals with an innovative energy management strategy for hybrid electric vehicle parallel drivetrains by exploiting an integrated multi-drives system.

Thanks to a suitable modeling for the induction machine, supercapacitors and batteries, an optimal vector control strategy is proposed to improve the energy efficiency of the system while taking into consideration the technical constraints related to the energy storage technologies in each possible operating scenario. A good agreement between simulations and experimental results has been achieved.

REFERENCES

[1] A. Castaings, W. Lhomme, R. Trigui and A.Bouscayrol, "Comparison of energy management strategies of a battery/supercapacitors system for electric vehicle under real-time constraints," in Applied Energy, vol. 163, Elsevier, Feb. 2016, pp. 190–200.

[2] Z. Song, H. Hofmann, J. Li, J. Hou, X. Han and M. Ouyang, "Energy management strategies comparison for electric vehicles with hybrid energy storage system," in Applied Energy, vol. 134, Elsevier, Dec. 2014, pp. 321–331.

[3] A. Tani, M. B. Camara and B. Dakyo, "Energy Management Based on Frequency Approach for Hybrid Electric Vehicle Applications: Fuel-Cell/Lithium-Battery and Ultracapacitors," IEEE Trans. Vehicular Technology, vol. 61, no. 8, pp. 3375-3386, Oct. 2012.

[4] J. O. Estima, A. J. M. Cardoso, "Efficiency Analysis of Drive Train Topologies Applied to Electric/Hybrid Vehicles," IEEE Trans. Vehicular Technology, vol. 61, no. 3, pp. 1021-1031, Mar. 2012.

[5] W. Shabbir, S. A. Evangelou, "Real-time control strategy to maximize hybrid electric vehicle powertrain efficiency," in Applied Energy, vol. 135, Elsevier, Dec. 2014, pp. 512–522.

[6] J. Kessels, M. Koot, P. van den Bosch, D. Kok, "Online Energy Management for Hybrid Electric Vehicles," IEEE Trans. Vehicular Technology, vol. 57, no. 6, pp. 3428-3440, Nov. 2008.

[7] G. Scarcella, G. Scelba, M. Cacciato, A. Spampinato, M. M. Harbaugh, "Vector Control Strategy for Multidirectional Power Flow in Integrated Multidrives Starter-Alternator Applications," IEEE Trans. Industry Applications, vol. 52, no. 6, pp. 4816-4826, Dec. 2016.

[8] M. Pulvirenti, G. Scarcella, G. Scelba, M. Cacciato, A. Testa, "Fault-tolerant AC multidrive system," IEEE Journal of Emerging and Selected Topics in Power Electronics, vol. 2, issue 2, pp. 224-235, Jun. 2014.

[9] R. Attanasio, M. Cacciato, G. Scarcella, A. Consoli, A. Testa, F. Gennaro, "A novel converter system for fuel cell distributed energy generation," in Proc. 2005 IEEE Power Electronics Specialists Conf.

[10] G. Li, J. Zhang, H. He, "Battery SOC constraint comparison for predictive energy management of plug-in hybrid electric bus," in Applied Energy, vol. 194, Elsevier, May 2017, pp. 578–587.

[11] S. Cordiner, M. Galeotti, V. Mulone, M. Nobile, V. Rocco, "Trip-based SOC management for a plugin hybrid electric vehicle," in Applied Energy, vol. 164, Elsevier, Feb. 2016, pp. 891–905.

[12] M. Cacciato, C. Cavallaro, G. Scarcella, A. Testa, "Effects of connection cable lenght on conducted EMI in electric drives," in Proc. 1999 IEEE Electric Machines and Drives Intenational Conf.

[13] S. Castano, L. Gauchia and J. Sanz-Feito, "Effect of Packaging on Supercapacitors Strings Modeling: Proposal of Functional Unit Defined Around Balancing Circuit," IEEE Trans. Components, Packaging and Manufacturing Technology, vol. 3, no. 8, pp. 1390–1398, Aug. 2013.

[14] V. Herrera, A. Milo, H. Gaztanaga, I. Etxeberria Otadui, I. Villarreal, H. Camblong, "Adaptive energy management strategy and optimal sizing applied on a battery-supercapacitor based tramway," in Applied Energy, vol. 169, Elsevier, May. 2016, pp. 831–845.

[15] D. Rotenberg, A. Vahidi and I. Kolmanovsky, "Ultracapacitor Assisted Powertrains: Modeling, Control, Sizing, and the Impact on Fuel Economy," IEEE Trans. Control Systems, vol. 19, no. 3, May 2011.

[16] S. M. Mousavi and M. Nikdel, "Various battery models for various simulation studies and applications," in Renewable and Sustainable Energy Reviews, vol. 32, Elsevier, Apr. 2014, pp. 477–485.

[17] W. Wang, H. Shu-Hung Chung, J. Zhang, "Near-Real-Time Parameter Estimation of an Electrical Battery Model With Multiple Time Constants and SOC-Dependent Capacitance," IEEE Trans. Power Electronics, vol. 29, no. 11, pp. 5905–5920, Nov. 2014.

[18] H. He, R. Xiong, H. Guo, and S. Li, "Comparison study on the battery models used for the energy management of batteries in EVs," in Energy Conversion and Management, vol. 64, Elsevier, Dec. 2012, pp. 113–121.

[19] M. Cacciato, G. Nobile, G. Scarcella, G. Scelba and A.G. Sciacca, "Energy management optimization in stand-alone power supplies using online estimation of battery SOC," in Proc. 2016 IEEE Power Electronics and Applications European Conf.

[20] G. L. Plett, "High-performance battery-pack power estimation using a dynamic cell model," IEEE Trans. Vehicular Technology, vol. 53, issue 5, pp. 1586-1593, Sep. 2004.

[21] M. Cugnet and B. Y. Liaw, "Effect of discharge rate on charging a lead-acid battery simulated by mathematical model," in Journal of Power Sources, vol. 196, Elsevier, Apr. 2011, pp. 3414–3419.

[22] S. Jier Huang, B. Ge Huang, F. Sheng Pai, "Fast Charge Strategy Based on the Characterization and Evaluation of $LiFePO_4$ Batteries," IEEE Trans. Power Electronics, vol. 28, no. 4, pp. 1555–1562, Apr. 2013.

[23] K. Itani, A. De Bernardinis, Z. Khatir, A. Jammal, M. Oueidat, "Regenerative Braking Modeling, Control, and Simulation of a Hybrid Energy Storage System for an Electric Vehicle in Extreme Conditions," IEEE Trans. Transp. Electrification, vol. 2, pp. 465-479, Dec. 2016.

[24] J. Zhang, Y. Yuan, C. Lv and Y. Li, "Modeling and Analysis of Regenerative Braking System for Electric Vehicle Based on AMESim," in Proc. 2015 IEEE Mechatronics and Automation International Conf.

[25] M. Cacciato, A. Consoli, G. Scarcella, G. Scelba, A. Testa, "Modified Space-Vector-Modulation Technique for common mode currents reduction and full utilization of the DC bus", in Proc. 2009 24th Annual IEEE Applied Power Electronics Conference and Exposition.